



Co-N-C in porous carbon with enhanced lithium ion storage properties

Shenghong Liu^{a,b}, Zhiping Lin^c, Feng Xiao^a, Jiakui Zhang^a, Dan Wang^d, Xianghong Chen^a, Yanming Zhao^{b,e}, Jiantie Xu^a^a Guangdong Provincial Key Laboratory of Atmospheric Environment and Pollution Control, National Engineering Laboratory for VOCs Pollution Control Technology and Equipment, School of Environment and Energy, South China University of Technology, Guangzhou 510640, China^b Guangdong Provincial Key Laboratory of Advanced Energy Storage Materials, School of Physics, South China University of Technology, Guangzhou 510640, China^c School of Physics and Optoelectronic Engineering, Guangdong University of Technology, Guangzhou 510006, China^d State Key Laboratory of Organic-Inorganic Composites, Beijing University of Chemical Technology, Beijing 100029, China^e South China Institute of Collaborative Innovation, Dongguan 523808, China

HIGHLIGHTS

- Co_n@N-C hybrids were prepared by a simple and efficient approach.
- Co_n@N-C hybrids display outstanding lithium storage properties.
- Co-N/N-C and porous structure are beneficial for transportation and storage of Li⁺.

ARTICLE INFO

Keywords:

Single atom cobalt

Co-N-C

Carbon

Anodes

Lithium ion batteries

ABSTRACT

Carbon materials as promising anodes for lithium ion batteries (LIBs) have attracted great attentions owing to their high theoretical capacities and rich natural resources. To improve anode performance of carbon, several common strategies have been developed, such as the fabrication of carbon with various nanostructures and modification of carbon frameworks by heteroatoms doping. Besides, the introduction of transition metal single atom or atom clusters embedded in nitrogen-doped carbon frameworks is also a feasible route. Herein, we report a simple and effective approach for synthesis of Co_n@N-C hybrids (*i.e.*, Co@N-C-0, Co_n@N-C-1 and Co_n@N-C-2) with interconnected porous carbon nanostructures and numerous active sites (*e.g.*, Co-N-C). When it was measured as anode for LIBs, the Co_n@N-C-1 hybrid displayed outstanding lithium storage properties with a high initial reversible capacity of 1587 mAh g⁻¹ at 0.1 C and maintained a high reversible capacity of 1000 mAh g⁻¹ at 5 C after 800 cycles. Both experimental and theoretical results reveal that Co-N-C with high specific activity along with interconnected porous carbon nanostructures synergistically promote the transportation and storage of Li⁺.

1. Introduction

With ever-growing application of lithium ion batteries (LIBs) in electric vehicles (EVs) and stationary energy-storage systems (ESSs), it requires LIBs with much higher energy and power densities [1]. The development of electrode materials is one key to large-scale application of high-performance LIBs. Although the graphite has dominated in LIB market since 1991, its low theoretical specific capacity of 372 mAh g⁻¹ and poor rate capability severely limit its application in EVs and EESS [2]. In order to replace the graphite, various promising anode candidates with high theoretical capacities have been widely explored, such as transition metal oxides/sulfides/carbides/nitrides (*i.e.*, Fe₂O₃, MoS₂, Ti₃C₂ and VN) [3–6], C-family based anodes (*i.e.*, carbon, Si, Ge, and

Sn) [7–9] and N-family anodes (*i.e.*, P, Sb and Bi) [10].

Among above-mentioned candidates, carbon materials have attracted great attentions due to their high theoretical capacities and rich natural resources. Unfortunately, carbon as anodes for LIBs still suffer from major obstacles, such as low initial Coulombic efficiency (CE) caused by the formation of a solid-electrolyte interphase (SEI) in the initial cycles and limited lithium storage properties. To offset the loss of lithium in the initial cycles, many efforts have been made to prelithiate the electrodes of LIBs, including electrochemical and chemical prelithiation, and the use of prelithiation additives (*e.g.*, Li₂O/Co, LiF and Li₂S) [11]. Apart from the progress achieved on the electrode prelithiation, the strategies to improve lithium storage properties of carbon mainly focus on the fabrication of various nanostructures (*e.g.*, hollow

E-mail addresses: zhaoyim@scut.edu.cn (Y. Zhao), jiantiexu@scut.edu.cn (J. Xu).<https://doi.org/10.1016/j.cej.2020.124377>

Received 13 December 2019; Received in revised form 24 January 2020; Accepted 6 February 2020

Available online 06 February 2020

1385-8947/ © 2020 Elsevier B.V. All rights reserved.

nanospheres, nanotubes and hierarchical nanostructures) [12], modification of carbon frameworks by heteroatoms (e.g., N, S, P) [13,14] doping and in combination of them have been commonly developed. The nanostructures endow carbon with large accessible surface area and pore volume, which are favorable for the quick penetration of electrolyte, rapid diffusion of ions and numerous active sites for Li^+ storage. The heteroatom doping enables carbon with the enhanced electronic and ionic conductivities, additional active sites for Li^+ storage, and better wettability between electrolyte and electrode. Recent studies have also revealed that transition metal (i.e., $\text{M} = \text{Fe}$ [15–17], Ni [18–20] and Co [21–23]) single atom (SA) or atom clusters embedded in nitrogen-doped carbon frameworks (M-N-C) demonstrate promising electrochemical properties in catalytic applications. This is because metal single atom/clusters not only could possess amazing electronic and reactive properties, but also max a theoretical 100% atom utilization efficiency [24]. In addition, the interaction between M and N is energetically favorable for the adsorption and reduction of charge/mass at M-N site. For example, based on their remarkable oxygen reduction reaction (ORR) activities, M-N-C as cathodes for various metal (e.g., Zn, Al and Li)-air batteries have been intensively reported so far [25–29]. Moreover, the M-N-C as cathodes for lithium sulfur batteries have also been found to deliver high capacity and cycling stability. This is not only due to the improved electrical conductivity of the hybrid, but also strong adsorption ability of lithium polysulfides between M-N-C and sulfur significantly reducing the “shuttle effect” of polysulfide during the cycles [30–32]. Compared to the progress achieved on M-N-C as cathodes for lithium batteries, however, the study on the atomic metal in carbon as anode for LIBs, as well as the interaction between Li^+ and M-N, is rarely scarce.

Herein, we developed a template-sacrificed approach to synthesize three-dimensional (3D) porous $\text{Co}_n\text{@N-C}$ (i.e., $\text{Co}_n\text{@N-C-1}$ and $\text{Co}_n\text{@N-C-2}$) hybrids consisting of atomically dispersed Co-N sites and Co atomic clusters by a thermal treatment method and subsequent acid leaching process. As a result, the $\text{Co}_n\text{@N-C}$ as anodes for LIBs exhibit outstanding lithium storage properties. Both experimental results and DFT calculations indicate that the outstanding anode performance is attributed to interconnected porous carbon nanostructures together with the formation of Co-N-C coordination centers serving as active sites to facilitate Li^+ storage/release.

2. Experimental

2.1. Synthesis of $\text{Co}_n\text{@N-C}$

SiO_2 nanospheres (50 nm) were purchased from Macklin without any other treatment. In a typical procedure, cobalt chloride hexahydrate ($\text{CoCl}_2 \cdot 6\text{H}_2\text{O}$, 200 mg), dicyanamide ($\text{C}_2\text{H}_4\text{N}_4$, 600 mg) and as-prepared SiO_2 nanospheres (100 mg) were mixed in *N*-methyl-2-pyrrolidone (NMP, 40 ml). The obtained mixtures were stirred and heated at 80 °C for several hours to form the bulk solids. After that, the solids were heated at 500 °C for 2 h and then heated up to 750 °C for 2 h at a temperature rate of 3 °C min^{-1} under Ar. Subsequently, the resulted samples were further leached in 0.15 M HF acid and washed using deionized water for several times to completely remove the SiO_2 spheres. Finally, the above samples were further treated with 0.5 M HCl overnight to remove excess Co. The resulted samples are denoted as $\text{Co}_n\text{@N-C-1}$. For comparison, the Co@N-C-0 and $\text{Co}_n\text{@N-C-2}$ samples were prepared by similar process with adding different amount of SiO_2 (0, 1, and 2 are corresponding to the use of 0, 100 and 200 mg SiO_2 , respectively). The scheme of synthesis process of $\text{Co}_n\text{@N-C}$ is illustrated in Fig. 1a.

2.2. Materials characterizations

The phases of $\text{Co}_n\text{@N-C}$ samples were analyzed using powder X-ray diffraction (XRD, Bruker D8 advance diffractometer) with Cu-K α

radiation ($\lambda = 1.5406 \text{ \AA}$). The morphologies of all samples were observed by scanning electron microscopy (SEM, JEOL JSM-6360LV) and transmission electron microscopy (TEM, FEI Titan G2 Themis). The thermogravimetric analysis (TGA, TA Instruments 2000) was carried out in air in the temperature range of 25–800 °C with a ramping rate of 10 °C min^{-1} . The surface chemistry and carbon states of the samples were analyzed by X-ray photoelectron spectra (XPS, Perkin-Elmer PHI X) and Raman spectrometer (Horiba), respectively. The specific surface area and pore distribution were calculated from the N_2 adsorption/desorption isotherms.

2.3. Electrochemical measurements

The electrochemical characterizations of the samples were performed using CR 2032 coin-type cells. For the preparation of working electrodes, a homogeneous slurry was obtained by mixing the active materials, carbon black and polyvinylidene difluoride binder, in a mass ratio of 8:1:1, respectively, with the NMP as the blending solvent. Then, the obtained slurry was uniformly coated on Cu foil, and then dried at 90 °C for 12 h in a vacuum oven. The mass of punched electrode pellet was controlled at $\sim 1.2 \text{ mg cm}^{-2}$. The cells were assembled in glove box with high-purity Ar-filled atmosphere using punched electrode as the cathode, lithium pellet as the counter and reference electrode, porous polypropylene as the separator and 1 M LiPF_6 in a mixture of EC/DEC (ethylene carbonate/diethyl carbonate, 1:2 (v/v)) as the electrolyte. The discharged/charged performance of the cells were evaluated using Land® battery tester system (Wuhan, China) in the voltage range of 0.01–3.0 V. Electrochemical impedance spectroscopy (EIS) and cyclic voltammetry (CV) were recorded on an AUTOLAB PGSTAT302N electrochemical workstation (Metrohm, Netherlands).

2.4. DFT calculation

DFT calculations were performed based on the density functional theory implemented in the VASP [33]. PBE pseudopotentials was used to describing the electron-ion interactions [34,35]. E_{cut} is set to 350 eV and allowed error in total energy is 10^{-4} . The k-point is $3 \times 3 \times 1$ in single-layer Graphene with 66 atoms. The vacuum region of 20 Å along with Z-axis direction is adopted to avoid interaction between images caused by periodic boundary conditions.

3. Results and discussion

SEM images of Co@N-C-0 (Fig. 1b) indicate that the Co@N-C-0 is composed by multi-walled carbon tubes with several micrometers length and $\sim 5 \text{ nm}$ thickness. Different from Co@N-C-0 , however, both $\text{Co}_n\text{@N-C-1}$ and $\text{Co}_n\text{@N-C-2}$ have their agglomeration patterns and sphere-like (Figs. 1e and S3a) in morphologies. Despite this, all elemental mappings of Co@N-C-0 (Fig. S1), $\text{Co}_n\text{@N-C-1}$ (Figs. 1h–k and S2), $\text{Co}_n\text{@N-C-2}$ (Fig. S3) clearly display the Co, N, C and O elements homogeneously distributed through the whole structure and no other impurities detected. The presence of Co in $\text{Co}_n\text{@N-C}$ suggests that the Co atoms/clusters are bonded with carbon and stable in a strong acid environment.

TEM images of Co@N-C-0 reveal that Co based nanoparticles (NPs) with a particle-size of 20 nm (Fig. 1c) and high crystallinity (Fig. 1d) are well encapsulated in carbon tubes. Fig. 1f and g (from magnified red rectangular area) show TEM images of $\text{Co}_n\text{@N-C-1}$. It can be seen that the hollow sphere carbon with a diameter of $\sim 100 \text{ nm}$ are interconnected to forming a 3D cross-linked carbon frameworks. This is attributed to the removal of stacked SiO_2 nanospheres during the acid leaching process. High resolution TEM (HR-TEM) image and selected area electron diffraction (SAED) pattern further reveal $\text{Co}_n\text{@N-C-1}$ with the amorphous pattern as well as small amounts of nanocrystal structures (Fig. 1l). As shown in inset of Fig. 1l, the lattice spacing of nanocrystal is estimated to be 0.20 nm, corresponding to the (1 1 1) of Co

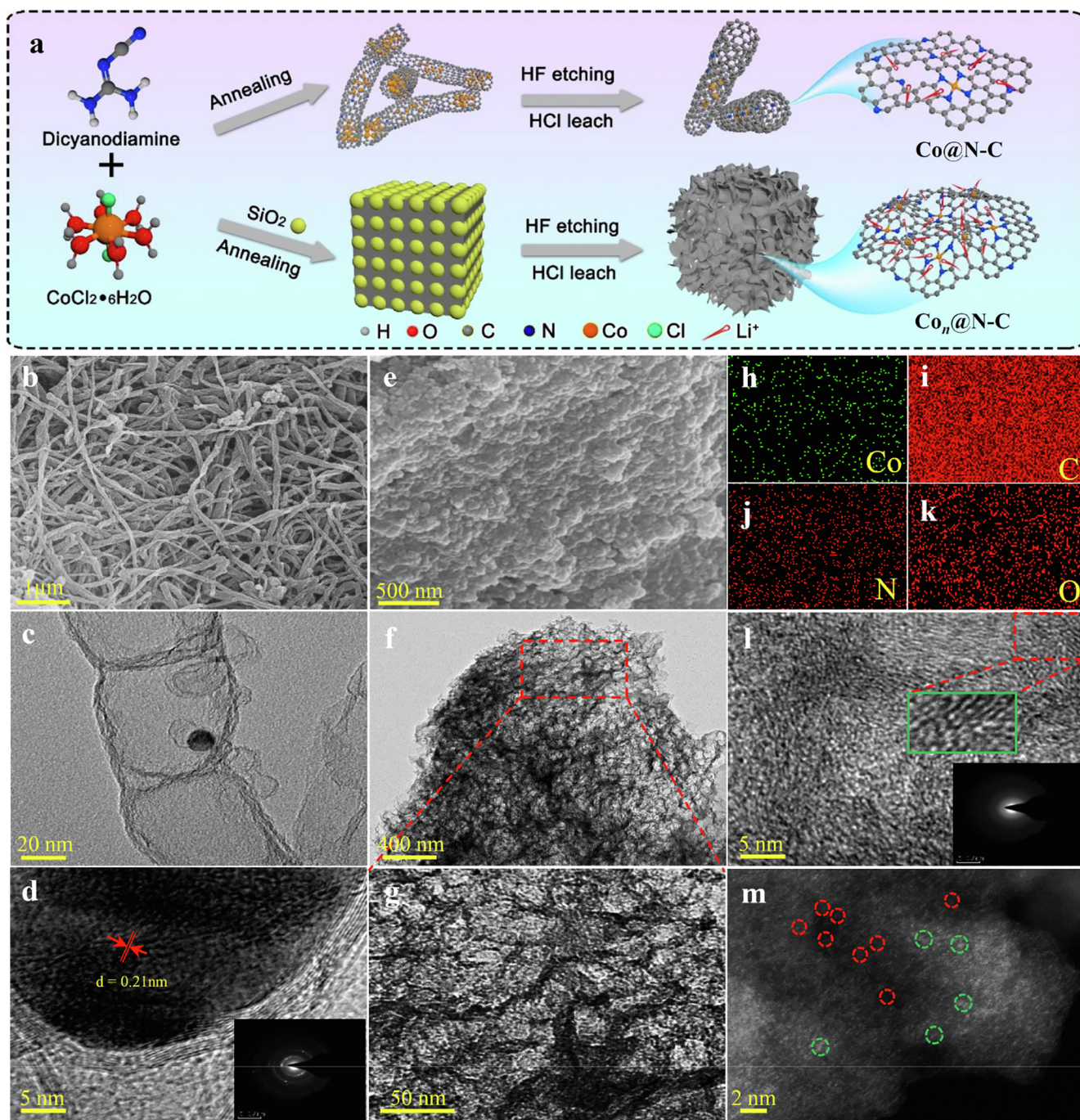


Fig. 1. (a) Illustration of the synthesis process of $\text{Co}_n\text{@N-C}$. SEM images of (b) Co@N-C-0 and (e) $\text{Co}_n\text{@N-C-1}$. Elemental mapping of Fig. 1e: (h) Co, (i) C, (j) N and (k) O. (c, d) TEM images of Co@N-C-0 . (f, g and l) TEM images and (m) HAADF-STEM image of $\text{Co}_n\text{@N-C-1}$. Insets of Fig. 1d and l: SAED of Fig. 1d and l.

[36]. To determine the detailed structure at atomic scale of $\text{Co}_n\text{@N-C-1}$, advanced spherical aberration-corrected electron microscopy was employed. As atomic-resolution aberration corrected high-angle annular dark field scanning transmission electron microscopy (HAADF-STEM) image (Fig. 1m) shown, the $\text{Co}_n\text{@N-C-1}$ presents a number of bright spots in a bar range of 0.2–1 nm uniformly dispersed on the carbon matrix, which should belong to SA-Co (red circles) and Co clusters (green circles). It can be deduced that the existence of SA-Co and Co clusters are most likely due to the breaking of Si–O–Co bond at the interfaces between SiO_2 and Co during the removal of SiO_2 process. This is also consistent with the formation of part discontinuous lattice (red-dot rectangle in Fig. 1l). Such point defects could be regarded as active sites for ions storage [37].

Fig. S4 compares XRD patterns of Co@N-C-0 , $\text{Co}_n\text{@N-C-1}$ and $\text{Co}_n\text{@N-C-2}$ before the acid leaching. As can be seen, all the samples have major Co NPs (ICSD #52934) rather than CoO_x . Even after acid treatment, the Co@N-C-0 remains the existence of the Co NPs (ICSD #52934) in the carbon matrix, which is consistent with the SEM and TEM observation (Fig. 1c and d). Different from that in Co@N-C-0 , there is no existence of Co NPs found in $\text{Co}_n\text{@N-C-1}$ and $\text{Co}_n\text{@N-C-2}$. This is due to the SiO_2 template leading the Co NPs initially formed on the carbon surface in an open framework, which is easy to be removed in the following leaching process. As a result, both $\text{Co}_n\text{@N-C-1}$ and $\text{Co}_n\text{@N-C-2}$ (Fig. 2a) display a broad XRD peak at $\sim 26.5^\circ$, corresponding to an amorphous carbon pattern [24]. Raman spectra of Co@N-C-0 , $\text{Co}_n\text{@N-C-1}$ and $\text{Co}_n\text{@N-C-2}$ (Fig. 2b) show all samples with two

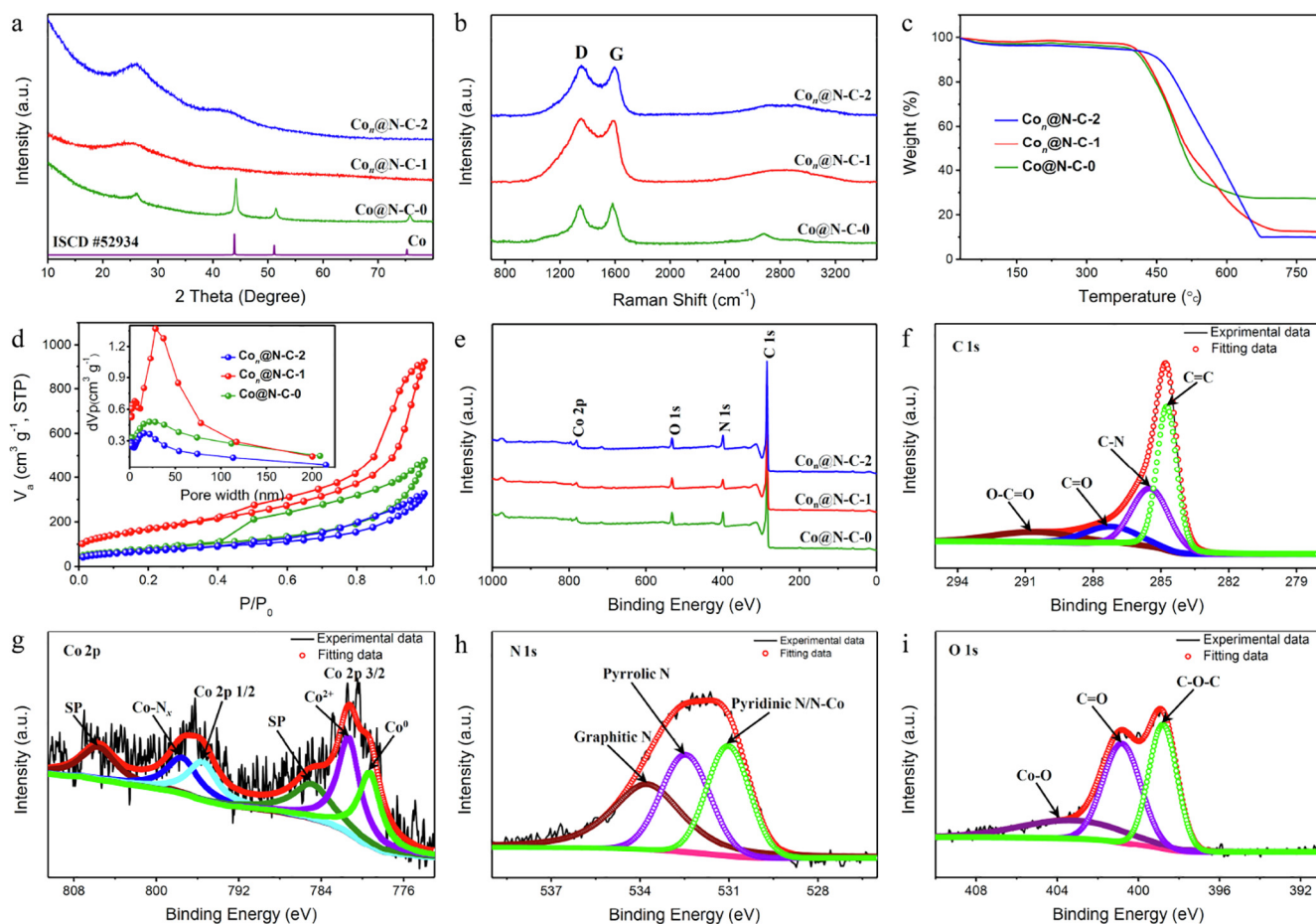


Fig. 2. (a) XRD patterns, (b) Raman spectra, (c) TGA curves, (d) N_2 adsorption-desorption isotherms, and (e) XPS spectra of Co@N-C-0, Co_n@N-C-1 and Co_n@N-C-2. High-resolution XPS spectra of Co_n@N-C-1: (f) C 1s, (g) Co 2p, (h) N 1s and (i) O 1s. Inset of Fig. 2d: pore size distributions of Co@N-C-0, Co_n@N-C-1 and Co_n@N-C-2.

characteristic D and G band located at ~ 1350 and ~ 1595 cm^{-1} , corresponding to the defects/disorder and graphitic carbon, respectively [38]. The intensity ratio of I_D/I_G for Co_n@N-C-1 (1.04) and Co_n@N-C-2 (1.02) are higher than that for Co@N-C-0 (0.94), indicating more amounts of defects in the carbon matrix induced by etching SiO₂ template.

In order to estimate the carbon content, TGA measurements were carried out in air. As shown in Fig. 2c, the Co@N-C-2 has a higher decomposition temperature compared to Co_n@N-C-1 and Co@N-C-0. This is most likely due to its lower surface area as well as plenty of Co-N-C, which make heat diffusion and carbon left difficult, and thus leading to a high decomposition temperature. Based on the detailed calculation in ESI (Fig. S5 and Eqs. (S1)–(S3)), the carbon contents of Co@N-C (Co@N-C-0, Co_n@N-C-1 and Co_n@N-C-2) are 79.6, 90.7 and 92.6 wt%, respectively [39]. The specific area and pore size distribution of the samples are determined by the BET method. As determined by nitrogen adsorption/desorption isotherms (Fig. 2d), the Co_n@N-C-1 shows a higher surface area of 597.1 m^2 g^{-1} than Co@N-C-0 (284.6 m^2 g^{-1}) and Co_n@N-C-2 (252.1 m^2 g^{-1}). Meanwhile, the Co@N-C-1 (1.37 cm^3 g^{-1} , 28.0 nm) exhibits a larger pore volume and mesopore size than Co@N-C-2 (0.38 cm^3 g^{-1} , 15.2 nm) and Co@N-C-0 (0.48 cm^3 g^{-1} , 21.2 nm). This is due to the use of SiO₂ as the template and an optimized mass ratio of SiO₂/(CoCl₂ and C₂H₄N₄) as the starting materials. It should be noted that the excessive use of SiO₂ (i.e., Co_n@N-C-2) could probably lead to the precursor agglomeration and then the decreased surface area after the removal of SiO₂. Overall, the larger surface area and pore volume are favorable for the electrolyte penetration and ions transportation (storage).

XPS survey was performed to analyse the elemental compositions

and their oxidation states of Co@N-C-0, Co_n@N-C-1 and Co_n@N-C-2. As shown in Fig. 2e, the full XPS surveys confirm the presence of C, N, O and Co elements in the hybrids, as evidenced by the XPS peaks of C 1s at ~ 284 eV, N 1s at ~ 400 eV, O 1s at ~ 532 eV and Co 2p at ~ 780 eV. According to the XPS analysis, the Co element contents in the Co@N-C-0, Co_n@N-C-1 and Co_n@N-C-2 are 0.59, 0.83 and 0.77 at.%, respectively. Other element contents (C, N and O) are listed in Table S1. The low content level of Co is probably attributed to the XPS technique with limited detection depth and Co mostly encapsulated by thick carbon shells. In order to more accurately estimate the Co content, the samples were dissolved by acid and inductively coupled plasma optical emission spectrometry (ICP-OES) analysis. It was found that the Co_n@N-C-1 and Co_n@N-C-2 had much lower Co content of 1.52 at.% and 1.41 at.%, respectively, than Co@N-C-0 (4.41 at.%). Such results together with XPS results suggest Co NPs well encapsulated in carbon matrix of Co@N-C-0. The content levels of Co_n@N-C-1 and Co_n@N-C-2 are similar to the TGA results and close to the single-atom catalysts distributing through carbon reported previously [40–43].

Figs. 2f–i and S6 demonstrate high resolution XPS spectra of the hybrids. It can be seen that the C 1s spectra can be splitted into four peaks: C=C at 284.7 eV, C–N at 285.5 eV, C=O at 287.3 eV and O–C=O at 290.8 eV. The Co 2p spectra (Figs. 1g and S6) are deconvoluted into Co 2p_{3/2} and 2p_{1/2}, Co(II), Co-N and the satellite peaks [44]. The satellite peaks locate at 785.7 and 805.6 eV. The peak at 779.3 eV is attributed to the zero-valent Co (Co⁰). The Co 2p_{3/2} at 781.3 eV and Co 2p_{1/2} at 795.5 eV are due to the surface oxidation of the hybrid. It should be noted that the Co-N at 797.5 eV verifies the formation of Co-N bond, which is resistant to acid etching in a certain extent [36,45]. Many reports have indicated that the catalysts containing uniformly

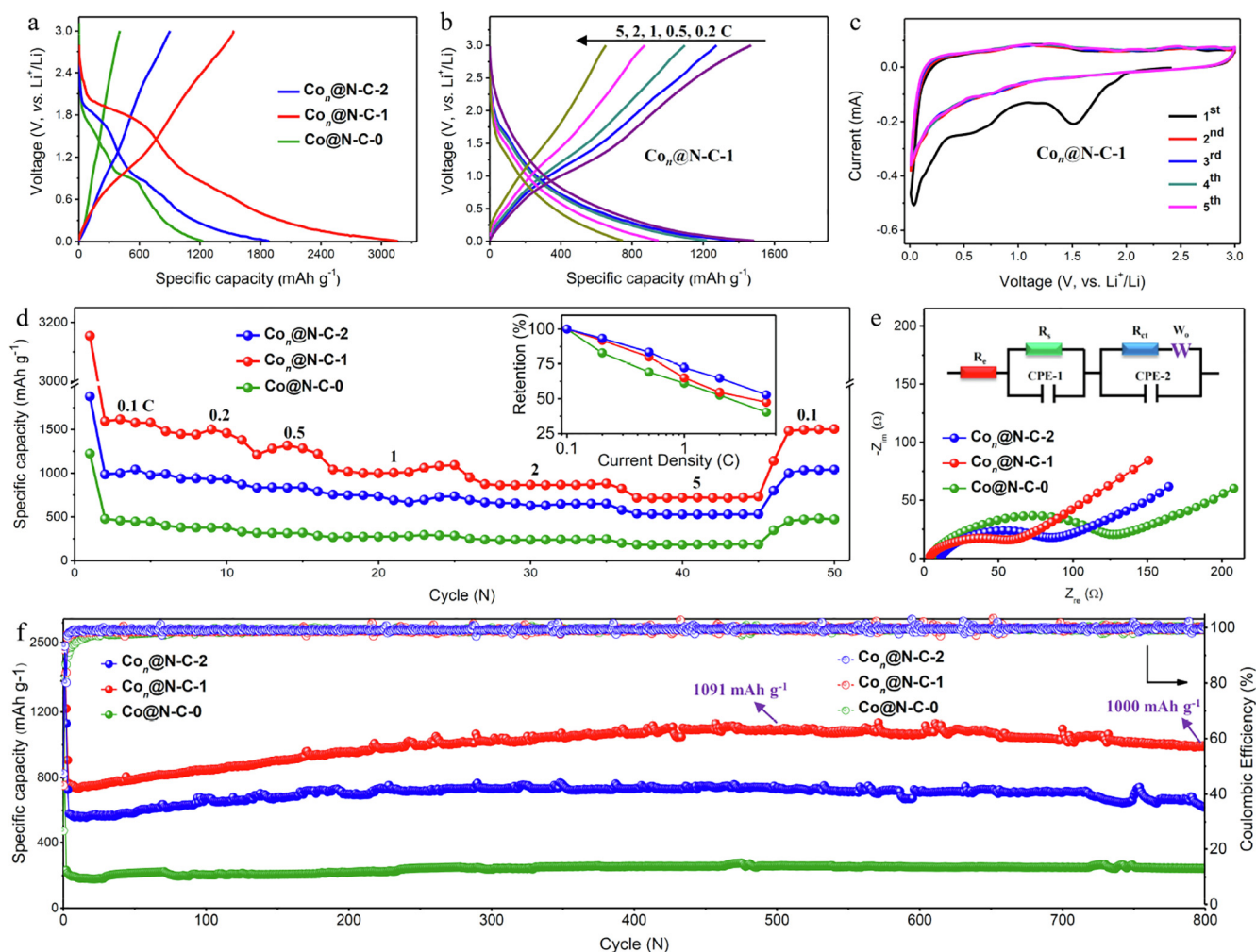


Fig. 3. (a) the 1st discharge-charge profiles at 0.1 C, (b) discharge/charge profiles at various C-rates, (c) CV curves at 0.1 mV s⁻¹ for initial five cycles, (d) rate capability, (e) electrochemical impedance spectra after 800 cycles and (f) cycling performance at 5 C of Co@N-C-0, Co_n@N-C-1 and Co_n@N-C-2. Inset of Fig. 3d: Capacity retention vs. different C-rates.

distributed Co-N moieties could significantly promote the catalytic properties [22,24,46,47]. This is mainly due to the Co-N can serve as active sites to facilitate the adsorption and transfer of mass (e.g., O₂, Li⁺, H⁺, OH⁻ and H₂O). In addition to the results from Co XPS peak, the Co-N bond can be also observed from the fitted pyridinic peak of N/Co at ~398.8 eV, along with other two typical N peaks of pyrrolic N (~400.8 eV), and graphitic N (~403.5 eV), from the N 1s spectra. The presence of N is originally from the raw material of dicyanamide.

Fig. 3a reproduces the 1st discharge-charge profiles of Co@N-C-0, Co_n@N-C-1 and Co_n@N-C-2 measured at 0.1 C (1 C = 372 mAh g⁻¹) between 0.01 and 3 V. Compared to Co@N-C-0, both Co_n@N-C-1 and Co_n@N-C-2 exhibit two more obvious plateaus at ~0.6 and ~1.6 V in the initial discharge process. After measurement at 0.1 C, the discharge-charge profiles of all samples at various C-rates from 0.2 to 5 C are shown in Figs. 3b and S7. As can be seen, the discharge-charge profiles of Co_n@N-C-1 and Co_n@N-C-2, similar to that of Co@N-C-0, are typical electrochemical behavior of carbonaceous materials [48]. Such electrochemical behaviours are further confirmed by cyclic voltammetry (CV) measurement of Co_n@N-C-1 and Co_n@N-C-2 at a scan rate of 0.1 mV s⁻¹ for initial five cycles (Figs. 3c, and S7). During the first cathodic scan, the irreversible reduction peaks at ~1.6 and ~0.6 V are ascribed to the decomposition of electrolytes and the formation of solid electrolyte interfaces (SEI) and the Li⁺ storage mainly occurs at below 0.6 V [49–51]. Notably, unlike many reported carbon materials as anodes for LIBs [52–54], the Co_n@N-C display an unusual reduction peak

at ~1.6 V. This should belong to the Co NPs and Co-N-C activating preliminary decomposition of electrolytes and the formation of SEI films [49,50]. Moreover, the Co_n@N-C-1 and Co_n@N-C-2 presents larger reduction peaks at 1.6 V than Co@N-C-0, indicating the stronger catalytic activity of Co-N-C than Co NPs. In addition, the Co_n@N-C-1 also shows stronger “capacitive” pattern than “intercalation” pattern due to its higher surface area. This is evidenced by no obvious oxidation peak in the characteristic “intercalation” voltage region at ~0.1 V compared to Co_n@N-C-2 and Co@N-C-0 (Figs. S7b and f). In the subsequent 4 cycles, the disappearance of the reduction peaks at ~0.6 and ~1.6 V, as well as highly overlapped CV curves, further confirm the formation of a strong and stable SEI film on the electrode surfaces in the first cycle and excellent cycling stability of the electrodes during the cycles.

Fig. 3d shows rate capability of the electrodes at various C-rates from 0.1 to 5 C. At 0.1 C, the Co_n@N-C-1 and Co_n@N-C-2 deliver high initial reversible capacities of 1587 and 903 mAh g⁻¹ with initial Coulombic efficiencies (CEs) of 48.6% and 48.1%, respectively. In spite of the low initial CEs of the Co_n@N-C-1 and Co_n@N-C-2, they are still higher than 33.3% for the Co@N-C-0 with an initial discharge capacity of 407 mAh g⁻¹. As the C-rate gradually increases from 0.1 to 5 C, the Co_n@N-C-1 delivers the highest average reversible capacities of 1459 (0.2 C), 1289 (0.5 C), 1027 (1 C), 877 (2 C) and 750 (5 C) mAh g⁻¹ among all the electrodes. Compared to Co@N-C-0, the Co_n@N-C-1 together with Co_n@N-C-2 also exhibit excellent rate capability (inset of

Fig. 3d). This could be attributed to more rich porous structures of $\text{Co}_n\text{@N-C}$ than Co@N-C-0 . Since the C-rate is switched back to 0.1 C, all the electrodes exhibit good reversibility, as evidenced by their reversible capacities close to the values at initial cycles.

To evaluate long-term cycling stability of the Co@N-C-0 , $\text{Co}_n\text{@N-C-1}$ and $\text{Co}_n\text{@N-C-2}$ electrodes, the cells were discharged-charged at 5 C for 800 cycles (Fig. 3f). Before the long-term cycling, the electrodes were activated at 0.1 C for two cycles. As can be seen, the activated $\text{Co}_n\text{@N-C-1}$ and $\text{Co}_n\text{@N-C-2}$ electrodes measured at 5 C could still maintain a high reversible capacities of 760 and 583 mAh g^{-1} in the third cycle. Over the rest long-term cycles, the $\text{Co}_n\text{@N-C-1}$ experiences a gradual increase in capacity and reaches the highest reversible capacities of 1091 mAh g^{-1} after 500 cycles. The ever-growing capacities are attributed to the carbon nanostructure with higher specific surface area, and rich mesopores, leading to the electrolyte-electrode activation at a relatively high C-rates [55–57]. After 800 cycles, a high reversible capacity of 1000 mAh g^{-1} without evident capacity decay can be still observed from the $\text{Co}_n\text{@N-C-1}$ electrode, further indicating its excellent cycling stability. Compared to $\text{Co}_n\text{@N-C-2}$, $\text{Co}_n\text{@N-C-1}$ displays higher reversible capacity over 800 cycles mainly due to its higher surface area of $\text{Co}_n\text{@N-C-1}$ (597.1 $\text{m}^2 \text{g}^{-1}$) than $\text{Co}_n\text{@N-C-2}$ (252.1 $\text{m}^2 \text{g}^{-1}$), and more rich Co-N active sites ($\text{Co}_n\text{@N-C-1}$ (13.70%) than $\text{Co}_n\text{@N-C-2}$ (10.86%) as evidenced by XPS. Despite the large differences in capacity, cycling stability, and rate capability, both $\text{Co}_n\text{@N-C-1}$ and $\text{Co}_n\text{@N-C-2}$ electrodes present high average CE approaching 99.0% over 500 cycles. As examined by electrochemical impedance spectra (EIS), the electrode kinetic of the Co@N-C-0 , $\text{Co}_n\text{@N-C-1}$ and $\text{Co}_n\text{@N-C-2}$ electrodes before cycling and after 800 cycles were compared in Figs. 3e and S8, 9. The detailed analysis information and fabricated equivalent model (inset of Fig. 3e) are summarized in ESI. Fitting results indicate that the charge-transfer kinetics-controlled resistance (R_{ct}), a key indicator of electrode kinetics, of $\text{Co}_n\text{@N-C-1}$ and $\text{Co}_n\text{@N-C-2}$ are apparently reduced from 50.4 and 90.5 Ω to 33.7 and 54.2 Ω , respectively, once again confirming the electrolyte-electrode activation of $\text{Co}_n\text{@N-C}$.

In order to better understand the lithium storage mechanism of the $\text{Co}_n\text{@N-C}$, we performed density functional theory (DFT) calculations in Figs. 4 and S10–S14 [33,34]. As can be seen, three different structure models (i.e., graphene (G), nitrogen doped graphene (N-G) and $\text{Co}_n\text{@N-C}$, Fig. 4a–c) and their interaction with Li^+ ion (Fig. 4d–f) are

configured. Based on the calculation, the $\text{Co}_n\text{@N-C}$ exhibits the larger Li adsorption energy (−1.43 eV) than N-G (−0.95 eV) and G (−0.93 eV), indicating its stronger Li^+ adsorption ability [58,59]. Moreover, it was also found that there are about 0.03–0.04 electrons transferred to nearby N atoms or C atoms in the model of $\text{Co}_n\text{@N-C}$ during the Li^+ adsorption, which is larger than those in G (0.01e) and N-G (0.01–0.02e). It indicates that the Co doping makes electron transfer in the Co-N-C more favorable. Along with Li^+ adsorption, the change of N–C bond length in Li1-site (0.0168 Å) and Li2-site (0.0181 Å) in the model of $\text{Co}_n\text{@N-C}$ is also smaller than that of NG (0.0173 Å and 0.0187 Å), as shown in Table S2. The less change of bond length between N and C atoms in the $\text{Co}_n\text{@N-C}$ during the lithiation-delithiation process could facilitate the stability of Co-N-C structures, leading to the cycling stability of electrode.

4. Conclusions

In conclusion, we have developed a simple and effective approach to the synthesis of $\text{Co}_n\text{@N-C}$ hybrids (i.e., $\text{Co}_n\text{@N-C-1}$ and $\text{Co}_n\text{@N-C-2}$) with single Co atom and small Co clusters. The Co atoms and clusters are well-distributed through three-dimensional (3D) interconnected N-doped carbon framework. When it was used as anodes for LIBs, the $\text{Co}_n\text{@N-C-1}$ hybrid displayed outstanding lithium storage properties with a high initial reversible capacity of 1587 mAh g^{-1} at 0.1 C and a high reversible capacity of 1000 mAh g^{-1} at 5 C after 800 cycles. This is because that the 3D interconnected N-doped carbon framework Co-N are not only favorable for the quick penetration of electrolyte and rapid diffusion of Li^+ , but also provide numerous active sites (e.g., Co-N-C) with high specific activity and large accessible surface area for Li^+ storage. As expected, the approach to synthesis of $\text{Co}_n\text{@N-C}$ could pave an important way to design other metals (M)-N-C as anodes toward high-performance LIBs in future.

Declaration of Competing Interest

The authors declare that they have no known competing financial interests or personal relationships that could have appeared to influence the work reported in this paper.

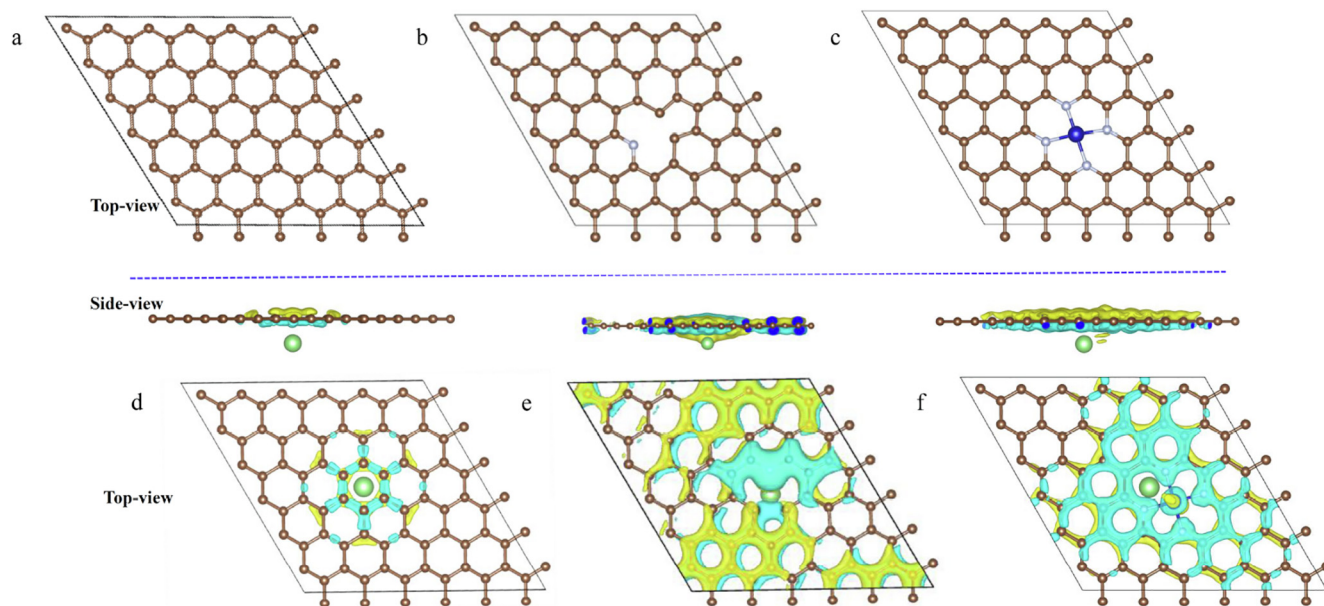


Fig. 4. Top views of (a) G, (b) N-G, and (c) $\text{Co}_n\text{@N-C}$; charge density differences of (d) G, (e) NG, and (f) $\text{Co}_n\text{@N-C}$ with one Li atom adsorbed. The yellow and blue represents the charge accumulate and loss regions. (For interpretation of the references to colour in this figure legend, the reader is referred to the web version of this article.)

Acknowledgements

The authors are grateful for financial support from the “Young Talent Fellowship” program through South China University of Technology, China; the Fundamental Research Funds for the Central Universities (2018JQ06, China); the Foundation (No. 2017B030308005, No. 2018A030313272) supported through the Science and Technology Bureau of Guangdong Government, the project (No. 2019622163008) of the Science and Technology Bureau from Dongguan Government and Grant (No. 51672086) through NSFC, China.

Appendix A. Supplementary data

Supplementary data to this article can be found online at <https://doi.org/10.1016/j.cej.2020.124377>.

References

- [1] J.W. Choi, D. Aurbach, Promise and reality of post-lithium-ion batteries with high energy densities, *Nat. Rev. Mater.* 1 (2016) 16013.
- [2] L. Croguennec, M.R. Palacin, Recent achievements on inorganic electrode materials for lithium-ion batteries, *J. Am. Chem. Soc.* 137 (2015) 3140–3156.
- [3] P. Poizot, S. Laruelle, S. Grugeon, L. Dupont, J.M. Tarascon, Nano-sized transition-metal oxides as negative-electrode materials for lithium-ion batteries, *Nature* 407 (2000) 496.
- [4] X. Xu, W. Liu, Y. Kim, J. Cho, Nanostructured transition metal sulfides for lithium ion batteries: progress and challenges, *Nano Today* 9 (2014) 604–630.
- [5] B. Anasori, M.R. Lukatskaya, Y. Gogotsi, 2D metal carbides and nitrides (MXenes) for energy storage, *Nat. Rev. Mater.* 2 (2017) 16098.
- [6] C. Wei, H. Fei, Y. Tian, Y. An, G. Zeng, J. Feng, Y. Qian, Room-temperature liquid metal confined in MXene paper as a flexible, freestanding, and binder-free anode for next-generation lithium-ion batteries, *Small* (2019).
- [7] R. Raccichini, A. Varzi, S. Passerini, B. Scrosati, The role of graphene for electrochemical energy storage, *Nat. Mater.* 14 (2015) 271.
- [8] W. Li, X. Sun, Y. Yu, Ge-Si-, Sn-based anode materials for lithium-ion batteries: from structure design to electrochemical performance, *Small Methods* 1 (2017) 1600037.
- [9] Y. An, H. Fei, G. Zeng, L. Ci, S. Xiong, J. Feng, Y. Qian, Green, scalable, and controllable fabrication of nanoporous silicon from commercial alloy precursors for high-energy lithium-ion batteries, *ACS Nano* 12 (2018) 4993–5002.
- [10] M.N. Obrovac, V.L. Chevrier, Alloy negative electrodes for Li-ion batteries, *Chem. Rev.* 114 (2014) 11444–11502.
- [11] F. Holstiege, P. Bärnmann, R. Nölle, M. Winter, T. Placke, Pre-lithiation strategies for rechargeable energy storage technologies: concepts, promises and challenges, *Batteries* 4 (2018) 4.
- [12] N.A. Kashedikar, J. Maier, Lithium storage in carbon nanostructures, *Adv. Mater.* 21 (2009) 2664–2680.
- [13] J.P. Paraknowitsch, A. Thomas, Doping carbons beyond nitrogen: an overview of advanced heteroatom doped carbons with boron, sulphur and phosphorus for energy applications, *Energy Environ. Sci.* 6 (2013) 2839–2855.
- [14] X. Wang, G. Sun, P. Routh, D.-H. Kim, W. Huang, P. Chen, Heteroatom-doped graphene materials: syntheses, properties and applications, *Chem. Soc. Rev.* 43 (2014) 7067–7098.
- [15] P. Chen, T. Zhou, L. Xing, K. Xu, Y. Tong, H. Xie, L. Zhang, W. Yan, W. Chu, C. Wu, Atomically dispersed iron-nitrogen species as electrocatalysts for bifunctional oxygen evolution and reduction reactions, *Angew. Chem. Int. Ed.* 56 (2017) 610–614.
- [16] S. Li, C. Cheng, X. Zhao, J. Schmidt, A. Thomas, Active salt/silica-templated 2D mesoporous FeCo-N_x-carbon as bifunctional oxygen electrodes for zinc-air batteries, *Angew. Chem. Int. Ed.* 57 (2018) 1856–1862.
- [17] Y. Li, H. Li, Y. Li, S. Peng, Y.H. Hu, Fe-B alloy coupled with Fe clusters as an efficient cocatalyst for photocatalytic hydrogen evolution, *Chem. Eng. J.* 344 (2018) 506–513.
- [18] S. Yang, T. Zhang, G. Li, L. Yang, J.Y. Lee, Facile synthesis of N/M/O (M = Fe Co, Ni) doped carbons for oxygen evolution catalysis in acid solution, *Energy Storage Mater.* 6 (2017) 140–148.
- [19] W. Liu, Y. Chen, H. Qi, L. Zhang, W. Yan, X. Liu, X. Yang, S. Miao, W. Wang, C. Liu, A durable nickel single-atom catalyst for hydrogenation reactions and cellulose valorization under harsh conditions, *Angew. Chem. Int. Ed.* 57 (2018) 7071–7075.
- [20] P. Lu, Y. Yang, J. Yao, M. Wang, S. Dipazir, M. Yuan, J. Zhang, X. Wang, Z. Xie, G. Zhang, Facile synthesis of single-nickel-atomic dispersed N-doped carbon framework for efficient electrochemical CO₂ reduction, *Appl. Catal. B: Environ.* 241 (2019) 113–119.
- [21] X. Zou, X. Huang, A. Goswami, R. Silva, B.R. Sathe, E. Mikmeková, T. Asefa, Cobalt-embedded nitrogen-rich carbon nanotubes efficiently catalyze hydrogen evolution reaction at all pH values, *Angew. Chem. Int. Ed.* 53 (2014) 4372–4376.
- [22] H.-W. Liang, S. Brüller, R. Dong, J. Zhang, X. Feng, K. Müllen, Molecular metal-N_x centres in porous carbon for electrocatalytic hydrogen evolution, *Nat. Commun.* 6 (2015) 7992.
- [23] X. Zhong, W. Yi, Y. Qu, L. Zhang, H. Bai, Y. Zhu, J. Wan, S. Chen, M. Yang, L. Huang, M. Gu, H. Pan, B. Xu, Co single-atom anchored on Co₃O₄ and nitrogen-doped active carbon toward bifunctional catalyst for zinc-air batteries, *Appl. Catal. B: Environ.* 260 (2020) 118188.
- [24] L. Fan, P.F. Liu, X. Yan, L. Gu, Z.Z. Yang, H.G. Yang, S. Qiu, X. Yao, Atomically isolated nickel species anchored on graphitized carbon for efficient hydrogen evolution electrocatalysis, *Nat. Commun.* 7 (2016) 10667.
- [25] J.-L. Shui, N.K. Karan, M. Balasubramanian, S.-Y. Li, D.-J. Liu, Fe/N/C composite in Li-O₂ battery: studies of catalytic structure and activity toward oxygen evolution reaction, *J. Am. Chem. Soc.* 134 (2012) 16654–16661.
- [26] F. Meng, H. Zhong, D. Bao, J. Yan, X. Zhang, In situ coupling of strung Co₂N and intertwined N-C fibers toward free-standing bifunctional cathode for robust, efficient, and flexible Zn-Air batteries, *J. Am. Chem. Soc.* 138 (2016) 10226–10231.
- [27] M. Yu, Z. Wang, C. Hou, Z. Wang, C. Liang, C. Zhao, Y. Tong, X. Lu, S. Yang, Nitrogen-doped Co₃O₄ mesoporous nanowire arrays as an additive-free air-cathode for flexible solid-state zinc-air batteries, *Adv. Mater.* 29 (2017) 1602868.
- [28] J. Gao, X. Cai, J. Wang, M. Hou, L. Lai, L. Zhang, Recent progress in hierarchically structured O₂-cathodes for Li-O₂ batteries, *Chem. Eng. J.* 352 (2018) 972–995.
- [29] W. Xie, Z. Li, S. Jiang, J. Li, M. Shao, M. Wei, Mass-loading independent electrocatalyst with high performance for oxygen reduction reaction and Zn-air battery based on Co-N-codoped carbon nanotube assembled microspheres, *Chem. Eng. J.* 373 (2019) 734–743.
- [30] X. Song, S. Wang, G. Chen, T. Gao, Y. Bao, L.-X. Ding, H. Wang, Fe-N-doped carbon nanofiber and graphene modified separator for lithium-sulfur batteries, *Chem. Eng. J.* 333 (2018) 564–571.
- [31] Z. Liu, L. Zhou, Q. Ge, R. Chen, M. Ni, W. Utetiawabo, X. Zhang, W. Yang, Atomic iron catalysis of polysulfide conversion in lithium-sulfur batteries, *ACS Appl. Mater. Interfaces* 10 (2018) 19311–19317.
- [32] M. Yu, S. Zhou, Z. Wang, Y. Wang, N. Zhang, S. Wang, J. Zhao, J. Qiu, Accelerating polysulfide redox conversion on bifunctional electrocatalytic electrode for stable Li-S batteries, *Energy Storage Mater.* 20 (2019) 98–107.
- [33] G. Kresse, J. Furthmüller, Efficient iterative schemes for ab initio total-energy calculations using a plane-wave basis set, *Phys. Rev. B* 54 (1996) 11169.
- [34] P.E. Blöchl, Projector augmented-wave method, *Phys. Rev. B* 50 (1994) 17953.
- [35] G. Kresse, J. Hafner, Ab initio molecular dynamics for open-shell transition metals, *Phys. Rev. B* 48 (1993) 13115.
- [36] W. Zhang, X. Yao, S. Zhou, X. Li, L. Li, Z. Yu, L. Gu, ZIF-8/ZIF-67-derived Co-N_x-embedded 1D porous carbon nanofibers with graphitic carbon-encased Co nanoparticles as an efficient bifunctional electrocatalyst, *Small* 14 (2018) 1800423.
- [37] S. Liu, F. Li, D. Wang, C. Huang, Y. Zhao, J.-B. Baek, J. Xu, 3D macroporous Mo₂C@N-C with incorporated Mo vacancies as anodes for high-performance lithium-ion batteries, *Small Methods* 2 (2018) 1800040.
- [38] M.S. Dresselhaus, A. Jorio, M. Hofmann, G. Dresselhaus, R. Saito, Perspectives on carbon nanotubes and graphene Raman spectroscopy, *Nano Lett.* 10 (2010) 751–758.
- [39] C. Cui, Z. Wei, J. Xu, Y. Zhang, S. Liu, H. Liu, M. Mao, S. Wang, J. Ma, S. Dou, Three-dimensional carbon frameworks enabling MoS₂ as anode for dual ion batteries with superior sodium storage properties, *Energy Storage Mater.* 15 (2018) 22–30.
- [40] B.-W. Zhang, T. Sheng, Y.-D. Liu, Y.-X. Wang, L. Zhang, W.-H. Lai, L. Wang, J. Yang, Q.-F. Gu, S.-L. Chou, H.-K. Liu, S.-X. Dou, Atomic cobalt as an efficient electrocatalyst in sulfur cathodes for superior room-temperature sodium-sulfur batteries, *Nat. Commun.* 9 (2018) 4082.
- [41] F. Li, G.-F. Han, H.-J. Noh, S.-J. Kim, Y. Lu, H.Y. Jeong, Z. Fu, J.-B. Baek, Boosting oxygen reduction catalysis with abundant copper single atom active sites, *Energy Environ. Sci.* 11 (2018) 2263–2269.
- [42] G. Han, Y. Zheng, X. Zhang, Z. Wang, Y. Gong, C. Du, M.N. Banis, Y.-M. Yiu, T.-K. Sham, L. Gu, Y. Sun, Y. Wang, J. Wang, Y. Gao, G. Yin, X. Sun, High loading single-atom Cu dispersed on graphene for efficient oxygen reduction reaction, *Nano Energy* 66 (2019) 104088.
- [43] J. Xie, B.-Q. Li, H.-J. Peng, Y.-W. Song, M. Zhao, X. Chen, Q. Zhang, J.-Q. Huang, Implanting atomic cobalt within mesoporous carbon toward highly stable lithium-sulfur batteries, *Adv. Mater.* 31 (2019) 1903813.
- [44] Q. Bai, F.-C. Shen, S.-L. Li, J. Liu, L.-Z. Dong, Z.-M. Wang, Y.-Q. Lan, Cobalt@nitrogen-doped porous carbon fiber derived from the electrospun fiber of bimetal-organic framework for highly active oxygen reduction, *Small Methods* (2018) 1800049.
- [45] W. Liu, L. Zhang, W. Yan, X. Liu, X. Yang, S. Miao, W. Wang, A. Wang, T. Zhang, Single-atom dispersed Co-N-C catalyst: structure identification and performance for hydrogenative coupling of nitroarenes, *Chem. Sci.* 7 (2016) 5758–5764.
- [46] Z. Du, X. Chen, W. Hu, C. Chuang, S. Xie, A. Hu, W. Yan, X. Kong, X. Wu, H. Ji, L.-J. Wan, Cobalt in nitrogen-doped graphene as single-atom catalyst for high-sulfur content lithium-sulfur batteries, *J. Am. Chem. Soc.* 141 (2019) 3977–3985.
- [47] C. Lei, Y. Wang, Y. Hou, P. Liu, J. Yang, T. Zhang, X. Zhuang, M. Chen, B. Yang, L. Lei, C. Yuan, M. Qiu, X. Feng, Efficient alkaline hydrogen evolution on atomically dispersed Ni-N_x species anchored porous carbon with embedded Ni nanoparticles by accelerating water dissociation kinetics, *Energy Environ. Sci.* 12 (2019) 149–156.
- [48] R. Raccichini, A. Varzi, S. Passerini, B. Scrosati, The role of graphene for electrochemical energy storage, *Nat. Mater.* 14 (2014) 271.
- [49] L. Su, Z. Zhou, P. Shen, Ni/C hierarchical nanostructures with Ni nanoparticles highly dispersed in N-containing carbon nanosheets: origin of Li storage capacity, *J. Phys. Chem. C* 116 (2012) 23974–23980.
- [50] L. Su, Y. Zhong, Z. Zhou, Role of transition metal nanoparticles in the extra lithium storage capacity of transition metal oxides: a case study of hierarchical core-shell Fe₃O₄@C and Fe@C microspheres, *J. Mater. Chem. A* 1 (2013) 15158–15166.
- [51] M. Du, D. Song, A. Huang, R. Chen, D. Jin, K. Rui, C. Zhang, J. Zhu, W. Huang,

- Stereoselectively assembled metal-organic framework (MOF) host for catalytic synthesis of carbon hybrids for alkaline-metal-ion batteries, *Angew. Chem. Int. Ed.* 131 (2019) 5361–5365.
- [52] M. Endo, C. Kim, K. Nishimura, T. Fujino, K. Miyashita, Recent development of carbon materials for Li ion batteries, *Carbon* 38 (2000) 183–197.
- [53] A.D. Roberts, X. Li, H. Zhang, Porous carbon spheres and monoliths: morphology control, pore size tuning and their applications as Li-ion battery anode materials, *Chem. Soc. Rev.* 43 (2014) 4341–4356.
- [54] W. Long, B. Fang, A. Ignaszak, Z. Wu, Y.-J. Wang, D. Wilkinson, Biomass-derived nanostructured carbons and their composites as anode materials for lithium ion batteries, *Chem. Soc. Rev.* 46 (2017) 7176–7190.
- [55] H. Sun, G. Xin, T. Hu, M. Yu, D. Shao, X. Sun, J. Lian, High-rate lithiation-induced reactivation of mesoporous hollow spheres for long-lived lithium-ion batteries, *Nat. Commun.* 5 (2014) 4526.
- [56] W. Wei, S. Yang, H. Zhou, I. Lieberwirth, X. Feng, K. Müllen, 3D graphene foams cross-linked with pre-encapsulated Fe₃O₄ nanospheres for enhanced lithium storage, *Adv. Mater.* 25 (2013) 2909–2914.
- [57] Y. Dou, J. Xu, B. Ruan, Q. Liu, Y. Pan, Z. Sun, S.X. Dou, Atomic layer-by-layer Co₃O₄/graphene composite for high performance lithium-ion batteries, *Adv. Energy Mater.* 6 (2016) 1501835.
- [58] C. Huang, J. Mahmood, Z. Wei, D. Wang, S. Liu, Y. Zhao, H.-J. Noh, J. Ma, J. Xu, J.-B. Baek, Metal (M = Ru, Pd and Co) embedded in C₂N with enhanced lithium storage properties, *Mater. Today Energy* (2019) 100359.
- [59] P. Zhai, T. Wang, W. Yang, S. Cui, P. Zhang, A. Nie, Q. Zhang, Y. Gong, Uniform lithium deposition assisted by single-atom doping toward high-performance lithium metal anodes, *Adv. Energy Mater.* 9 (2019) 1804019.